PERGAMON

Journal of Structural Geology 24 (2002) 123–143

JOURNAL OF STRUCTURAL GEOLOGY

www.elsevier.com/locate/jstrugeo

Internal structure of the Precordilleran fault system (Chile) — insights from structural and geophysical observations

C. Janssen[a,*], A. Hoffmann-Rothe[a], S. Tauber[b], H. Wilke[c]

[a]*GeoForschungsZentrum Potsdam, Telegrafenberg, D-14473 Potsdam, Germany*
[b]*Freie Universität Berlin, Geophysik, Malteserstrasse 74-100, D-1249 Berlin, Germany*
[c]*Univ. Catholica del Norte, Depto. Ciencas Geologicas, Antofagasta, Chile*

Received 9 August 2000; revised 13 March 2001; accepted 20 March 2001

Abstract

Geological field work and audiomagnetotelluric data from two profiles crossing the West Fissure Zone in northern Chile were used to describe the geometry and structure of the fracture damaged zone surrounding this strike-slip fault system. The W–E profiles show that the width of the West Fissure Zone based on the fracture density distribution derived from aerial photographs is 4000 m on profile A and 7000 m on profile B. The estimated widths correspond roughly to the region where the fault is kinematically uniform. The ratio of the fault width to the fault length ranges from 0.024 to 0.041. This ratio compares favourably with the measured ratio of small (metre-scale) natural faults.

Audio-frequency magnetotelluric imaging shows low electrical resistivity zones (resistivity of ~5–30 Ωm) coincident with the mapped surface traces of the fault. However, these zones are very narrow (width about 100 m) and only 50 m (profile A) and 200 m (profile B) deep, respectively. On profile B the shallow high conductive zone is underlain by a resistive zone (~1000 Ωm). The conductivity enhancement in these shallow and narrow zones contrasts with the broad process zone revealed by structural analysis. We assume that the conductivity enhancement is due to meteoric water entering a zone of ruptured rocks along the fault trace (fault core). At present, we have no indication for seismic slip along the investigated segments of the West Fissure Zone. Fault models have shown that during aseismic periods of fault evolution fault healing (i.e. strength recovery) due to compaction and cementation is active. Fluids and fluid transport, which are probably responsible for enhanced conductivity, are confined to the remaining fractures of the fault core at shallow depth.

Keywords: Brittle deformation; Fault; Fracture; Aerial photographs; Fault kinematics; Fault scaling relationship; Audio-frequency magnetotelluric imaging

1. Introduction

Brittle fault zones are lithologically heterogeneous and structurally anisotropic discontinuities in the upper crust (Caine et al., 1996). The shear strength of fault zones affects the rheological behaviour of the crust and controls the distribution of earthquakes. The kinematics and mechanics of faulting deformation may yield information on the rheological structure of the overriding plate in a subduction zone (Molnar, 1992). Within faults, several deformation mechanisms operate in conjunction and result in an alternation between weakening and strengthening processes. In particular, the observed weakness of some continental fault zones relative to the surrounding country rock may be fundamental to the mechanics of slip (Lachenbruch and Sass, 1980; Zoback et al., 1987).

Information on fault growth is contained within the structure of fault zones, specifically in the distribution of displacement along the fault and in the damaged zone around the main slip-surface (Shipton et al., 1997). Vermilye and Scholz (1998) distinguish between damaged zone (DZ) and fracture process zone (FPZ). The FPZ is defined as the volume of rock containing features that result directly from propagation of the fault tip, whereas the DZ integrated several episodes of faulting deformation (Chester and Logan, 1986). It is proposed here to use the term damaged zone because of the accumulated deformation surrounding the fault as a whole. The geometry and width of the FPZ or DZ are related to fault growth and consequently can be used to evaluate fault growth models. For instance, laboratory experiments and theoretical models indicate that the thickness of the process zone scales linearly with fault length and fault displacement (Cowie and Scholz, 1992; Scholz et al., 1993; Cowie and Shipton, 1998). Evaluation of these laboratory and experimental results are based mainly on field studies at microscopic scale (e.g. Anders and Wiltschko, 1994; Vermilye and Scholz, 1998; Vermilye

* Corresponding author.
E-mail address: jans@gfz-potsdam.de (C. Janssen).

0191-8141/02/$ - see front matter
PII: S0191-8141(01)00053-0

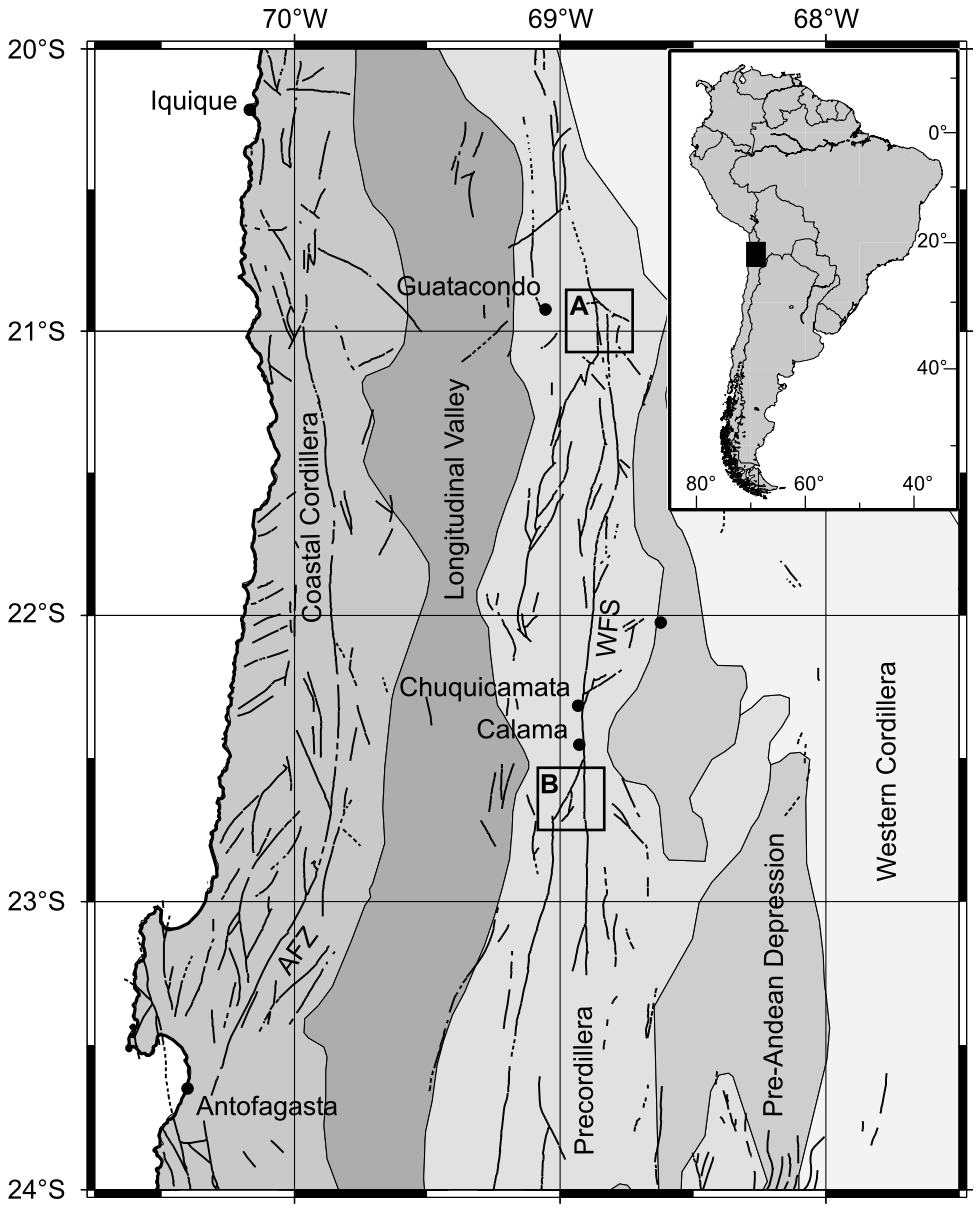

Fig. 1. Overview sketch of Northern Chile with morphological units and faults/lineaments according to Reutter et al. (1994). The profile locations are indicated by rectangular areas.

and Scholz, 1999). Little work has been done to investigate mesoscopic fault patterns at scales between metres and kilometres (Schulz and Evans, 2000). However, understanding of fault zone propagation, fluid circulation and earthquake nucleation requires detailed information about mesoscopic structures.

The present work focuses on this point. The questions arise accordingly: are fault scaling laws based on experiments and small-scale field studies valid for major strike slip faults? Do the observed mesoscopic fault patterns fit to recent models of fault evolution? Answering these questions requires knowledge concerning the geometry, kinematics and strength of the fault. The Andes of South America display some excellent examples of strike-slip zones in the fore-arc region that allow us to address the questions mentioned above. We examine the internal structure of the West Fissure Zone (WFZ, Chile; Fig. 1) using structural and audiomagnetotelluric (AMT) investigations. The geometry of the magnetotelluric anomalies across the fault provides crucial information on the lateral and vertical extent of fault zones, which are virtually unknown by structural methods (Unsworth et al., 1997, 1999, 2000). The first part of this paper presents detailed information about the variations of fault zone characteristics (thickness and depth of the damaged zone, deformation mechanisms, fault kinematics) both along and across the fault system. We then examine whether the variation of electrical conductivity corresponds with deformation intensity, fluid flow and/or other factors.

Based on these field observations and on the geometry of the magnetotelluric anomalies across the fault, we evaluate fault scaling relationships and consider our results in context with models of fault zone evolution. To achieve these goals we select two suitable profiles (A and B) normal to the WFZ (Fig. 1). A companion paper (in preparation) considers mechanical and geochemical fluid-rock interactions and fluid sources along the same two profiles.

2. Geological setting

Since the Lower Jurassic (~200 Ma, Andean cycle, Coira et al., 1982) the Pacific coast of the South American continent has been subjected to active tectonism. Deformation has been caused by the subduction of the Pacific Nazca-plate below South America. Plate convergence along the Central Andes trends NE to ENE with a moderate slab dip between 25 and 30° at a rate of 0.08 m/a. The direction and magnitude of the kinematic plate vector changed, leading to distinct deformation stages through time (Table 3 in Scheuber et al., 1994). Large NS-directed strike-slip fault zones (Precordilleran Fault system, PFS) have resulted from oblique collision (Beck, 1983; Reutter et al., 1991). These faults are composed of various regional segments, each having undergone a distinct series of deformation events (Lindsay et al., 1995). In the northern part of Chile the regional branch of the PFS is known as WFZ, West Fault or Falla Oeste. The fault system has influenced the emplacement and mineralization of porphyry-copper-related intrusions (Lindsay et al., 1995).

The WFZ is well exposed as a continuous structure along a 170 km zone extending from Calama northward to Quebrada Blanca (Fig. 1; Dilles et al., 1997). The fault zone has been active since the Late Eocene/Early Oligocene (Reutter et al., 1996). Most authors assume that an older dextral strike-slip motion caused by subduction-related magmatic arc tectonics of the Incaic tectonic phase was followed by sinistral shear corresponding to a time of reduced convergence rate (Reutter et al., 1996). The youngest event is the reactivation of dextral slip under the same kinematic conditions as described for the older phase. The tectonic inversion of the fault system is also reflected in varying amounts of displacement (dextral displacement: 0.5–2 km, sinistral displacement: 35–37 km; Reutter et al., 1991; Tomlinson et al., 1997a,b; see Section 3.3). Our investigation concentrates on two segments of the WFZ, between 20°54′–20°58′ S (profile A) and 22°30′–22°50′ S (profile B), respectively (rectangular areas in Fig. 1).

Profile A is located along the W–E trending Quebrada (valley) Guatacondo within the Precordillera (Fig. 2a). Here, the main trace of the WFZ separates Late Cretaceous–Paleocene coarse-grained sandstones and conglomerates from tuffs of the Cerro Empexa Formation (Albian–Cenomanian). Deformation structures, which include folds, foliations, brittle faults and thrusts, trend obliquely to the main fault trace (Carrasco et al., 1999). Profile B crosses the PFS where the WFZ splits into at least two branches (Fig. 2b). One branch turns to the south-southwest into the Limon Verde fault zone (LVZ). The LVZ separates early Paleozoic metamorphic rocks from younger (Permian, upper Paleozoic) igneous rocks (Baeza, 1984). The main branch of the WFZ continues southwards through the Limon Verde basement block. The central part of the block is composed of mainly granite–diorite with minor abundance of gabbro and metamorphic rocks (Lucassen et al., 1999). The deformation history is characterised by folding and faulting, which have not yet been studied in detail. The foliation strikes around north and the fold axes dip gently to the south (Baeza, 1984). Brittle deformation post-dated folding, as evidenced by cataclasites and fault breccias, which developed in rocks, folded directly before.

3. Structural patterns of faulting

3.1. Insights from aerial photographs

Aerial photographs (1:50,000) were used for fracture orientation and density determinations. A fracture is defined as any discontinuity that does not change orientation by more than 20° (Vermilye, 1996). Fracture densities (length in km per square km) in a given unit area (grid cell) of 0.25 km^2 and the degree in fracture orientation were measured using the line intersection method (Underwood, 1970). This method uses the intersections of the fractures with the grid lines of a regularly gridded area.

The analysis of the strike of fracture traces in the aerial photograph of profile A reveals two sets of fractures, namely NNW–SSE and NNE–SSW striking fractures (Fig. 3a and b). The WFZ cannot be recognised as a single main trace but as a number of distinct but inter-related fracture lines. The major directions are subparallel or form a low angle to the direction of the WFZ (rose diagram in Fig. 3b). According to our fieldwork we assume that these fracture sets are mainly secondary faults related to the WFZ. The regional (background) density ($\rho_b = 3.1\ km^{-1}$) was calculated from the averaged grid cell densities at greater distance from the fault trace. The highest fracture density ($\rho_h = 5.8\ km^{-1}$) was determined in the central portion of the fault, (upper row in the table of Fig. 3b; Table 1). The width of the fault (W_f) defined as the region where the fracture density exceeds the mean value ($\rho_x = 3.8\ km^{-1}$) is about 4000 m (Fig. 3c, see Discussion). Fracture density decreases with increasing distance to the fault with a slightly sharper decrease on the western side of the fault (Fig. 3c). The lower row in the table of Fig. 3b shows the degree of fracture orientation (scale of anisotropy) varying from 0% for no anisotropy to 36% for a partly oriented system of lines (intersection method; Underwood, 1970). These values show that the degree of fracture orientation is higher in

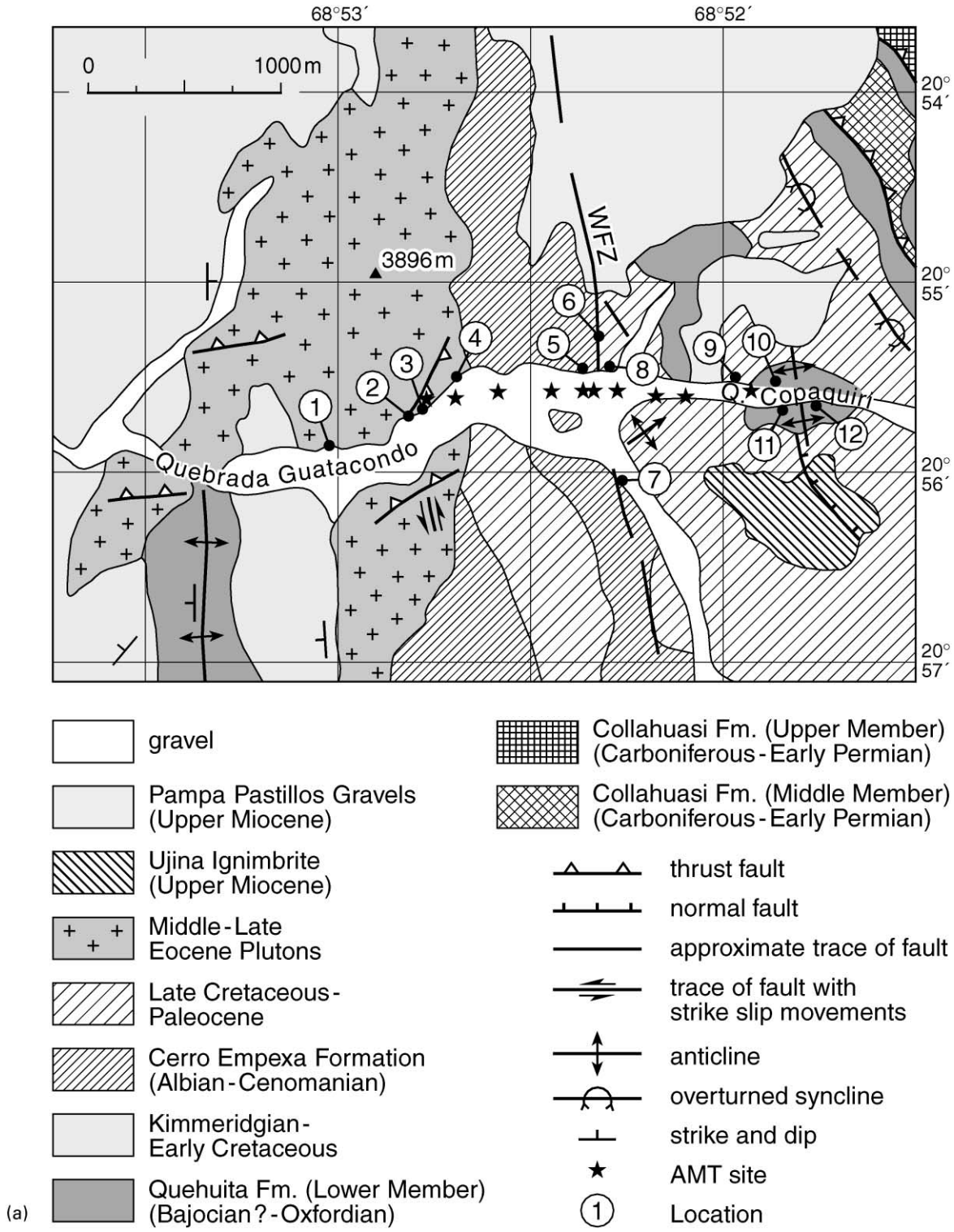

Fig. 2. Geological map of areas of detailed investigations. (a) Quebrada Guatacondo (slightly modified after Carrasco et al., 1999). (b) Limon Verde area (slightly modified after Boric et al., 1990). Asterisks indicate AMT sites.

the fault core compared with sites further away from the fault.

The analysis of 248 fracture lines in the aerial photograph of profile B (Fig. 4a) displays inter-related fractures tracing the WFZ and LVZ, respectively (Fig. 4b). The orientation data in the rose diagram (Fig. 4b) reveal a NE–SW maximum and two sub-maxima (NNW–SSE and NW–SE). The increase of fracture densities and the higher degree in fracture orientation towards the faults (WFZ, LVZ; Fig. 4b and c) confirms the result of profile A (Table 1). The broader

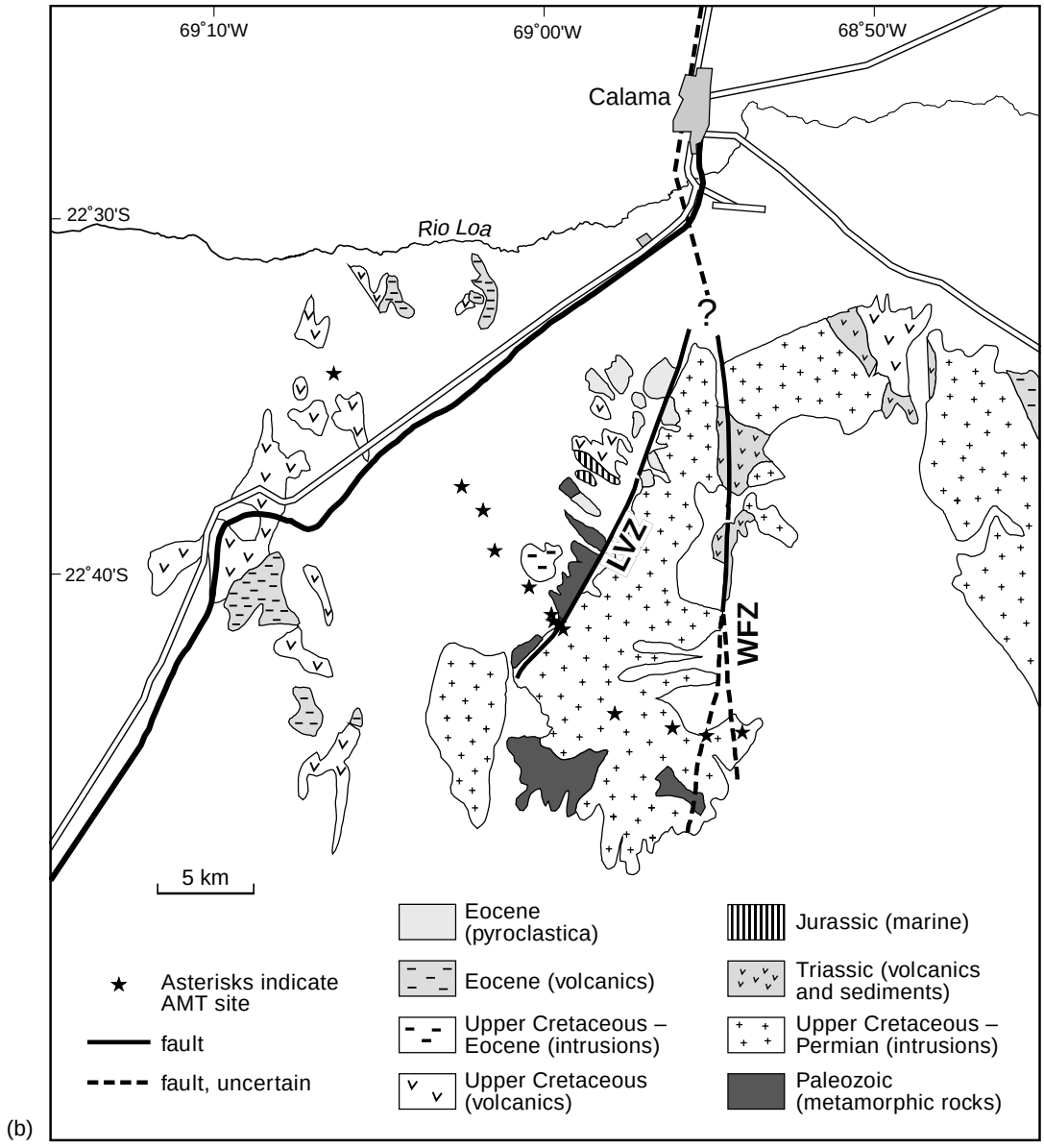

Fig. 2. (*continued*)

zone of increased densities (compared with profile A) is probably caused by the fact that in this area the fault splits into at least two branches.

3.2. Fault rocks, fracture and veins at outcrop scale

Fault-related deformation has not resulted in the formation of extensively faulted zones. In both profiles the fault core is only distinguished by the increase in subsidiary faults above regional levels (Fig. 5). Solely along these subsidiary faults we observe indications for a cataclastic progression toward the (minor) fault traces over a distance of a few centimetres (Fig. 6). The change between fractured host rock (fracture spacing >20 cm) and cataclasite is extremely sharp and distinct (Fig. 6a; compare Chester and Logan (1986) and Schulz and Evans (2000)). The cataclastic zone, ranging in thickness between 10 and 20 cm, consists of rocks that are friable and highly fractured at orientations parallel to the minor fault (Fig. 6b). Alteration processes are widespread, causing visible grain size reductions and erosion. Microscopically, fracturing, pressure solution and dissolution features are the dominant deformation mechanisms in the cataclastic zone (Fig. 6c). The fracture density increases and the fragment size decreases towards the centre of the cataclastic zone. In the central part, the cataclasite consists of a very fine-grained matrix (grain size <10 μm) and small host rock fragments (mainly quartz, Fig. 6c).

As determined at the outcrop scale, the fracture orientation varies among the different locations (Fig. 7). Along profile A, the fractures strike in the range 0–20° (30°), 50–70° and 160–180° with no significant differences

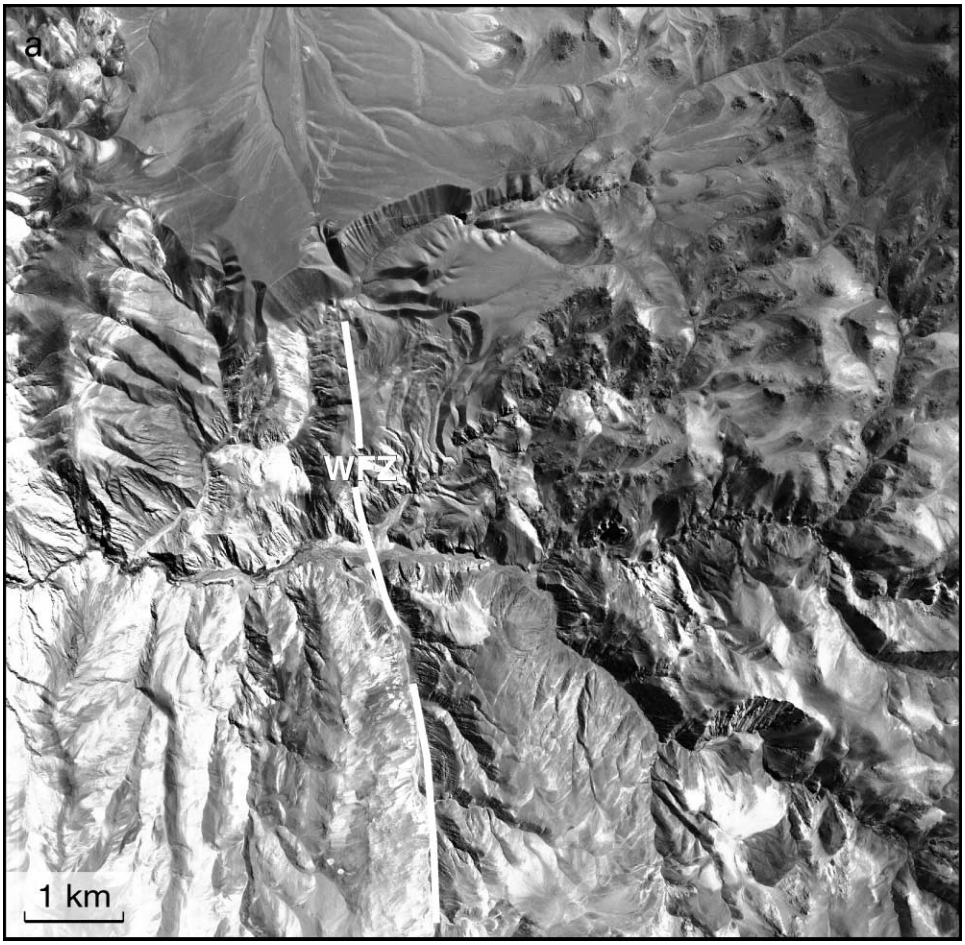

Fig. 3. Guatacondo area with West Fissure Zone (WFZ). (a) Aerial photograph of the investigated area of profile A. We observe 195 traces of fractures with a larger density around the fault. (b) Corresponding structural map with rose diagram of fracture-line orientation, table with fracture density distribution (upper row) and the degree of fracture orientation in percent (lower row). (c) Corresponding plot of crack density in dependence on fault distance (normal to the fault trace). ρ_x = mean value and ρ_h = peak value of fracture density.

between both sides of the fault (Fig. 7a). The major fracture direction NNE–SSW (NNW–SSE) is roughly sub-parallel to the WFZ. In contrast to Chester et al. (1993), our data cannot be used to infer the orientation of stress near the fault. The scattering in fracture orientation is independent from the fault plane distance. Calcite- and quartz-veins are barely visible in the investigated outcrops. The few found are mostly NE–SW oriented (Fig. 7b). Veins trending parallel or at low angles to the fault trace are less abundant. Calcite veins are composed of euhedral blocky calcite and calcites with fibrous habit. Fracturing, twinning and pressure solution are the dominant deformation mechanisms. Quartz veins are filled with coarse quartz cement. Microfractures and pressure solution are less common than in calcite veins.

The Limon Verde area (profile B) shows three similar fracture sets; NNE–SSW, ENE–WSW and NW–SE (NNW–SSE) oriented (Fig. 7c). Clear differences in fracture orientation between the vicinity of WFZ and LVZ are not recognisable. Veins in this study area are thin and mainly filled with quartz. However, their numbers are too small to analyse orientation and deformation characteristics.

3.3. Fault kinematics

Subsidiary faults with associated striations were measured in several outcrops along profile A and B (Fig. 8). Shortening and stretching directions were derived using the kinematic approach of Allmendinger (1989; see also Michel, 1994). From their geometrical relationship to the WFZ, most of the subsidiary faults are assumed to be synthetic Riedel-shears or H-fractures (i.e. hybrid planes, between Riedel and extensional fractures). Overprinting relationships, for example superposed striations on single fault planes, reveal two faulting events within the Guatacondo area (profile A, Fig. 8a and b).

The older faulting event is composed of two main sets of faults with some scattering in orientation. One set comprises faults trending N–S and NNE–SSW and, together with synthetic second-order faults, suggests sinistral movement. The other set with roughly E–W striking faults indicates

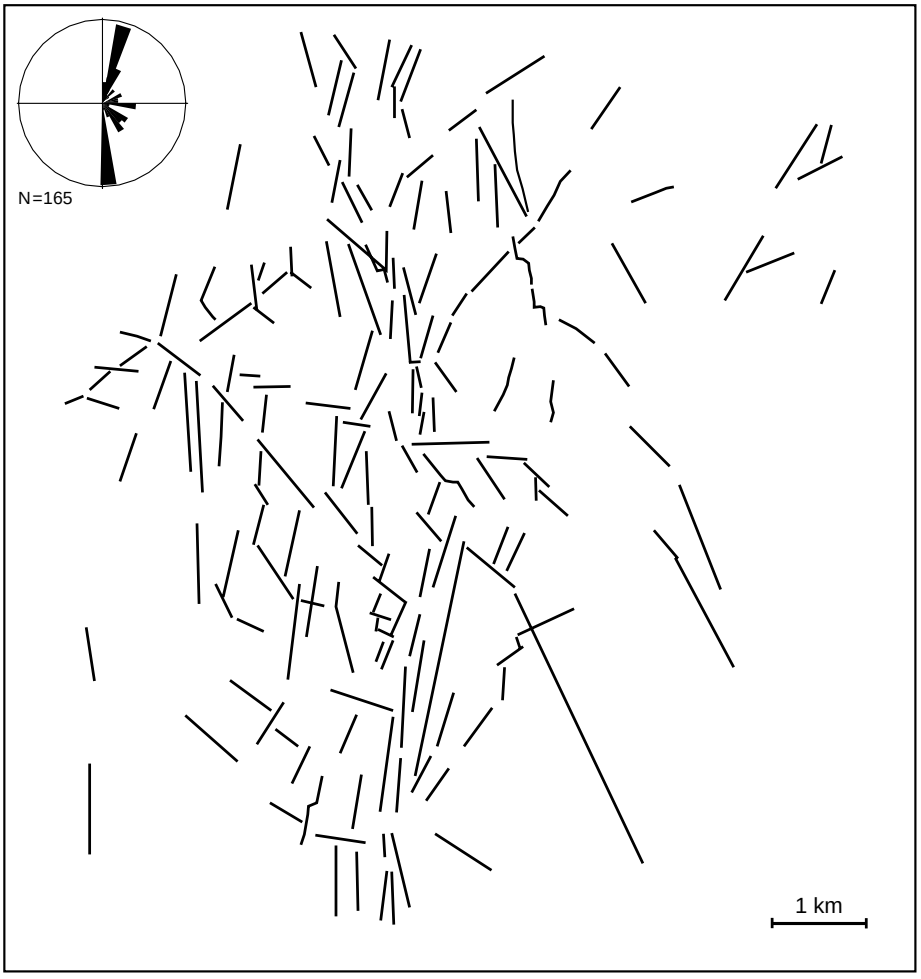

	3.1	3.1	3.1	3.8	3.8	3.7	4.3	5.8	4.0	4.3	3.4	3.1	3.1	3.1	3.1	3.1	3.1	3.1
	0	0	0	18%	18%	3%	21%	36%	5%	28%	9%	0	0	0	0	0	0	0

damaged zone *Core* *damaged zone*

(b)

WFZ

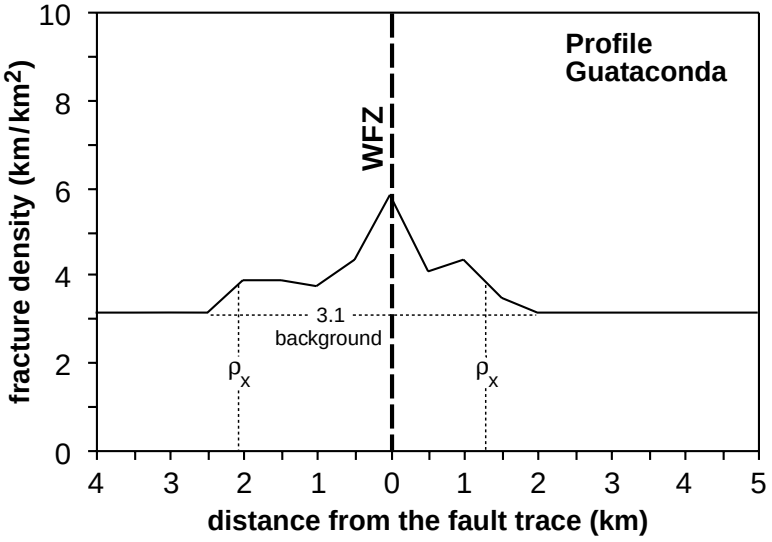

(c)

Fig. 3. (*continued*)

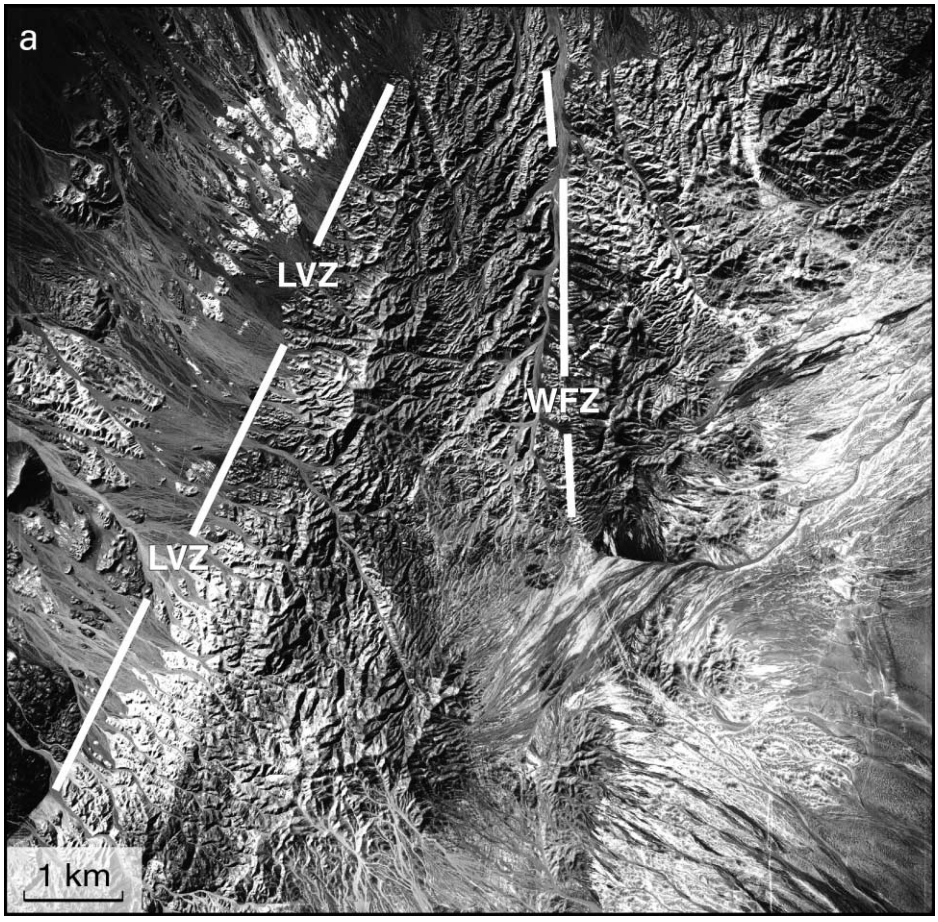

Fig. 4. Limon Verde area with WFZ and Limon Verde Fault Zone (LVZ). (a) Aerial photograph of the Limon Verde area. (b) Corresponding structural map with rose diagram of fracture-line orientation, table with fracture density distribution (upper row) and the degree of fracture orientation in percent (lower row). (c) Corresponding plot of crack density in dependence on fault distance (normal to the fault trace).

dextral movement. The derived shortening direction is NW–SE oriented (Fig. 8a). The orientation of principal strain axes is relatively constant on both sides of the fault. Further away from the main fault trace (100 m, 300 m, 800 m up to 1000 m) the composite strain axes once again indicate the same directions. The uniform orientation of principal strain axes suggests that the whole WFZ is kinematically coherent. At distances of about 1500 m from the main fault trace changes in the direction of principal strain axes of the older event were observed. The derived shortening direction rotates counter clockwise towards E–W. The older event is constrained by the age of an andesitic dike swarm (36.2 ± 0.6 Ma; Hammerschmidt et al., 1992), which cuts through the sedimentary sequence (Carrasco et al., 1999).

Younger faults, which occur only in few outcrops, form a pattern of NW–SE striking sinistral faults and NE–SW striking dextral faults. The derived composite shortening axes trend NE–SW (Fig. 8b). The upper limit of the younger deformation event is constrained by the age of the undeformed Ujina ignimbrites (9.0 ± 0.4 Ma; Vergara and Thomas, 1984) and ages of undeformed ignimbrites north of the investigated area (16.2 ± 0.2 MA; Muñoz and Sepulveda, 1992).

Within the area of profile B, subsidiary fault planes up to several tens of metres width cut through the brecciated material. Fault orientation scatter more than those in profile A, but two main fault sets dominate the fault pattern (Fig. 8c). One set comprises NW–SE to WNW–ESE sinistral fault planes and the other set is composed of ENE–WSW

Table 1
Geometry of the process zone and fault scaling relationships. ρ_x = mean value of fracture density; ρ_b = background value of fracture density; ρ_h = highest or peak value of fracture density; W_f = fault width; L = fault length; d = fault displacement

Profile	ρ_x (km^{-1})	ρ_b (km^{-1})	ρ_h (km^{-1})	W_f (km)	L (km)	W_f/L	d (km)
A	3.8	3.1	5.8	4	170	0.024	101
B	3.6	3.1	5.9	7	170	0.041	101

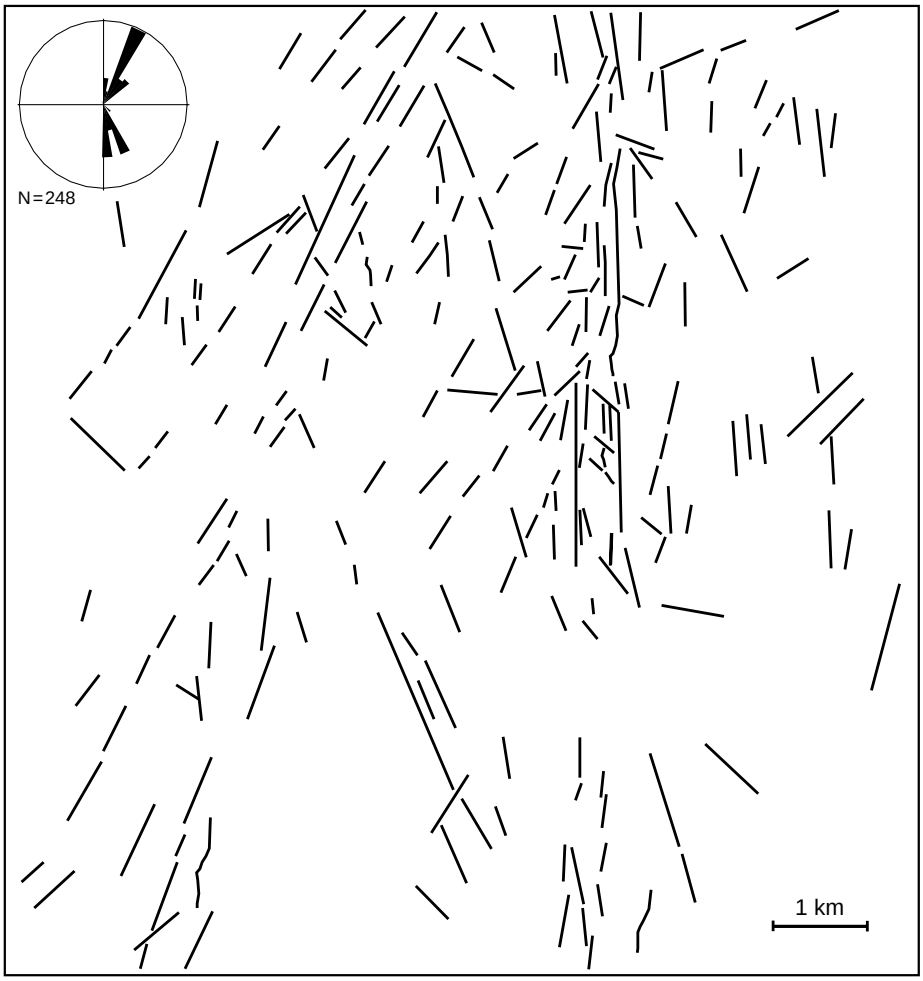

3.1	3.1	3.1	3.4	3.5	3.6	4.3	4.3	3.6	3.6	3.3	3.5	5.9	3.3	3.3	3.4	3.3	3.6	3.1
0	0	0	9%	11%	14%	28%	16%	14%	6%	6%	11%	32%	6%	6%	9%	6%	16%	0

damaged zone | Core | damaged zone | Core | damaged zone

LVZ WFZ

(b)

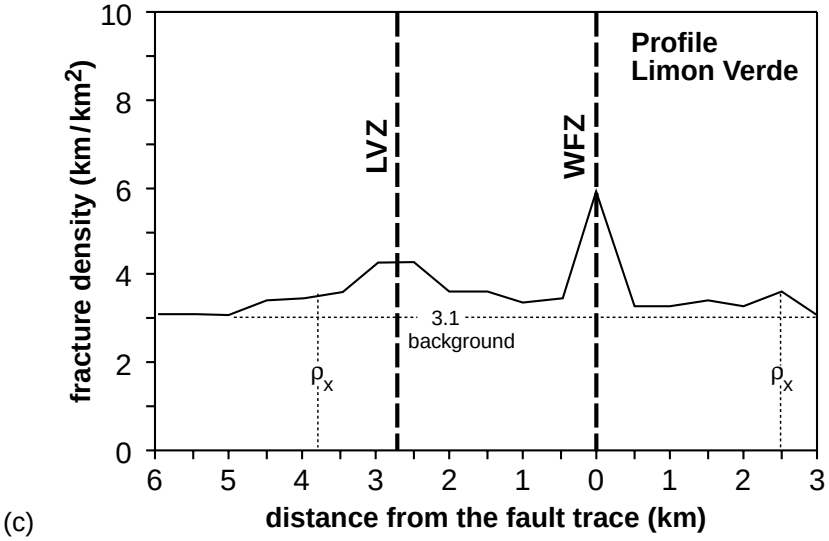

(c)

Fig. 4. (*continued*)

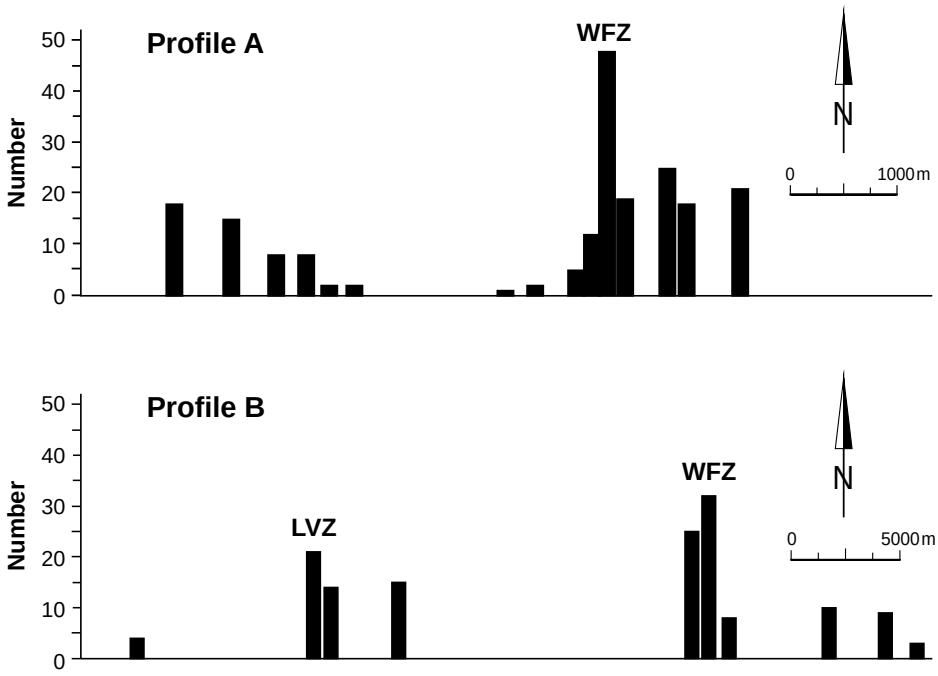

Fig. 5. Subsidiary fault frequency plotted against distance from the main fault trace (normal to the fault trace) for profiles A and B.

to E–W trending faults, indicating dextral movement. Rotation of the shortening directions is shown in relation to the fault distance (Fig. 8c). West of the LVZ the shortening directions are oriented NW–SE. They rotate toward the LVZ, exhibiting a roughly E–W orientation. Between LVZ and WFZ the derived composite strain axes once again indicate subhorizontal ±E–W shortening and ±N–S extension. Faults east of the WFZ, but still adjacent to the main fault trace, have the same orientation as those between the LVZ and WFZ. Even the derived strain axes do not change significantly. Further east from the WFZ (4–5 km) the shortening direction rotates to NE–SW.

4. Audio-frequency magnetotelluric imaging

The investigation of mesostructures described in the previous section does not allow an estimation of the fault geometry below the surface. Therefore, in conjunction with the structural observations two audiomagnetotelluric (AMT) surveys were carried out along E–W trending lines crossing the WFZ at ~20°54′ S (profile A) and 22°40′ S (profile B). Line A consists of 10 AMT sites along an approximately 1500 m profile (Plate 1a). The site separation within the area where the main fault deformation is visible at surface is 50 m. Profile B is 20 km long and comprises 12 sites and a remote reference site 10 km northwest of the profile. It crosses the LVZ and the WFZ, but due to topography (cf. Plate 2a) only the LVZ has been investigated in detail, i.e. with site separation down to 300 m.

4.1. Data acquisition and data characteristics

We recorded data in the frequency range of 1000–0.001 Hz. The penetration depth (radius) of the electromagnetic signals increases with decreasing frequency. Data analyses after Swift (1967) and Groom and Bailey (1989) reveals that within the frequency range of 1000–1 Hz the AMT data may be interpreted by two-dimensional (2-D) modelling. In the 2-D case the electric and magnetic fields in the ground are oriented parallel and perpendicular to the strike of the conductivity anomaly. The direction of the electric current flow parallel to the strike of the conducting feature is referred to by E-polarization (E-Pol or TE mode) while the orientation of the electric current perpendicular to strike is named B-polarization (B-Pol or TM mode). Since we expect the WFZ and the LVZ to produce a lateral conductivity contrast, AMT data should reflect the strike of the faults. The measurements were made in a geographic N–S and E–W coordinate system. An angular deviation between the measurement coordinate system and the electrical strike direction can be calculated from AMT observations (Swift, 1967; Groom and Bailey, 1989). These angles are shown in Fig. 9a–e (profile A) and Fig. 9f–k (profile B) in the form of polar histograms for five frequency bands.

Since the WFZ trends more or less N–S one would expect a dominant electric strike in the same direction. This is true for the frequency bands 1000–100 Hz (Fig. 9a), 100–10 Hz (Fig. 9b) and 10–1 Hz (Fig. 9c), where a main strike direction of about 5° W can be identified. However, the calculated strike angle has a 90° ambiguity (illustrated by

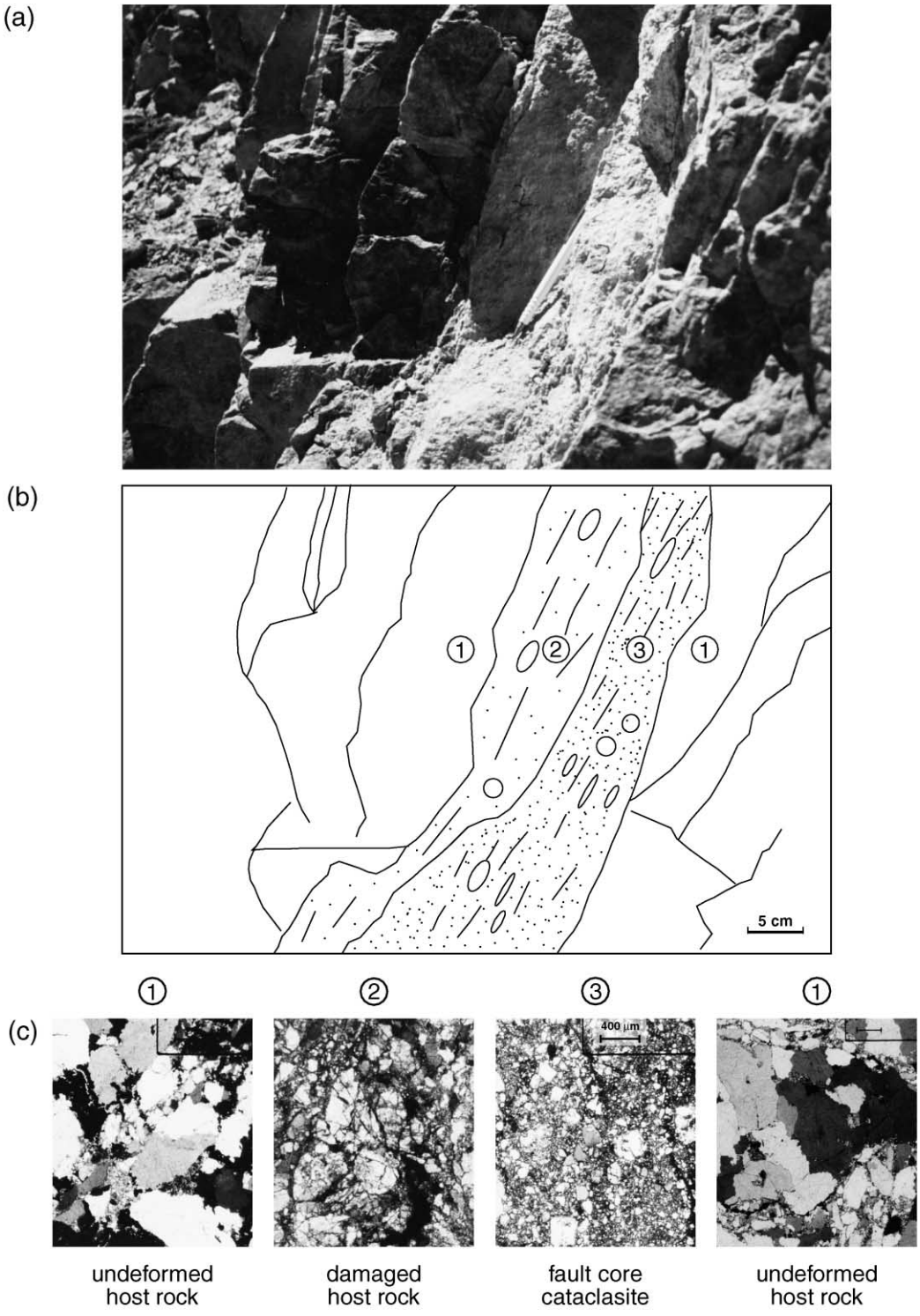

Fig. 6. Subsidiary fault with narrow zone of localized deformation. (a) Photograph of fault-related deformation patterns. Notice the cataclastic progression towards the (minor)-fault core. (b) Sketch of the photograph in (a). (c) Photomicrographs of unfaulted and faulted rocks showing the cataclastic progression towards the fault core. Scale bar is 100 μm, crossed nicols.

the grey directional roses in Fig. 9). The geology of this region gives no indication of an E–W strike direction and the topography of the Guatacondo canyon as a cause for such a strike can be ruled out because the penetration radius of the electromagnetic signal in the highest frequency band is shorter than the width of the canyon. For lower frequencies (i.e. greater depth of penetration; Fig. 9d and e) the strike shows a greater directional variability. The assumption of a simple 2-D conductivity geometry does not hold anymore. The data of profile A have subsequently been

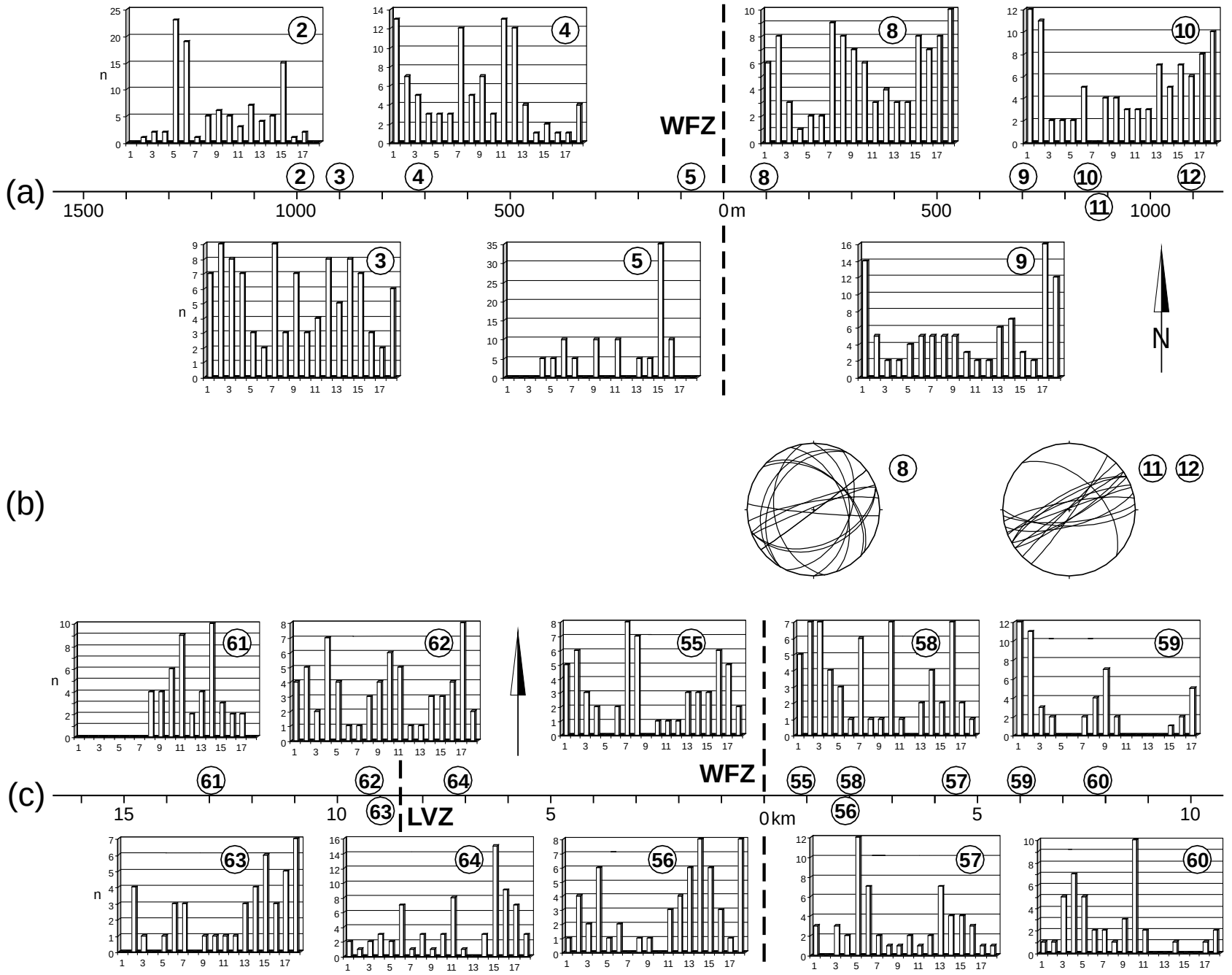
(a)
WFZ
n
2
4
8
10
3
5
9
N
1500
1000
500
0 m
500
1000
(b)
8
11
12
(c)
61
62
55
58
59
WFZ
LVZ
63
64
56
57
60
15
10
5
0 km
5
10

rotated by 5° W and are interpreted within a frequency range of 1000–1 Hz.

Profile B traverses both the WFZ and the LVZ. The strike angle distribution of the highest frequency band (1000–100 Hz; Fig. 9f) is bipolar, whereby the western sites show the N–S and the eastern sites the NNE–SSW strike direction of the WFZ and the LVZ, respectively. Within the next frequency band (100–10 Hz) strike orientation scatters around the N direction (Fig. 9g). In the medium frequency range of 10–1 Hz the strike distribution again resolves into separate orientations: the easternmost sites exhibit a NW–SE strike direction, whilst the majority follows a NNE–SSW trend (Fig. 9h). For lower frequencies (Fig. 9j and k) the strike angles rotate towards NNW–SSE. As a compromise an overall N–S strike direction has been adopted and un-rotated AMT data within the frequency range of 1000–1 Hz of profile B were subjected to 2-D modelling.

4.2. Two-dimensional modelling

The AMT data were inverted using two versions of the 2-D inversion algorithm by Mackie et al. (1997a). Joint and separate inversions of E- and B-polarization apparent resistivities and phases have been carried out for both profiles. Due to galvanic distortion (Jones, 1988) any individual site may be affected by static shift, which offsets the apparent resistivities of the E- and B-Pol by constant but arbitrary values, while the phases remain unaltered. Consequently, emphasis has been put on the inversion of the phase data by down-weighting the apparent resistivities. This was realized by either using a version of the inversion algorithm, which includes the calculation of static shift estimates (profile A) or by applying an elevated error-floor for the apparent resistivities (25%), which again has been drastically increased (towards infinity) for static shift suspected sites (profile B). The starting model for each inversion was a homogeneous half space.

The inversion yields to models with enhanced conductivity, confined to shallow depths, in place of the structurally defined WFZ and LVZ cores, respectively, if the E-Pol data are included. An inversion of B-Pol data on its own does not display a fault-related conductivity anomaly. This can be expected for a very narrow conductor because electric charges accumulate at the edges of the conductor. These charges have opposite signs and their effect cancels out at the surface.

On profile A the WFZ is imaged as a narrow (width: 100 m) low resistivity zone (C1 in Plate 1a; resistivities below 20 Ωm) within the top 50 m below the surface. It is important to note the absence of a deep reaching, good conducting zone, as it was imaged in several MT surveys crossing the San Andreas Fault (e.g. Parkfield; Unsworth, 1997, 1999, 2000). Starting the inversion with a more deeply extended good conducting zone, as an a priori information, produces worse fits. The conductive anomalies C2 and C3 and the resistive structures R of Plate 1a cannot be easily correlated to the geology visible at the surface. The transition of plutonic rocks to the Cretaceous to Paleocene succession of sandstones, tuffs and conglomerates falls into the position of the change in resistivity in the western part of the profile (C2), but a correlation remains speculative. A comparison of observed apparent resistivities and phases and the model response is shown as pseudo-sections against frequency for both polarizations in Plate 1d. The root-mean-square (rms) misfits for each site are presented in Plate 1b, adding up to an overall rms misfit of 2.05 (assuming an apparent resistivity error floor of 10% and phase error floor of 2°). Static shifts are estimated by the average ratio of observed and modelled apparent resistivities and are displayed in Plate 1c. Sites close to the fault trace display some static shift effects for the E-Pol apparent resistivities.

Profile B shows a similar, slightly less conductive anomaly (resistivities below 50 Ωm) within the upper 200 m in the position of the LVZ (C1 in inset Plate 2b). Again, no zone of enhanced conductivity has been detected at greater depth beneath the surface trace. Instead a high resistive zone is imaged with resistivities about 1000 Ωm. The significance of the resistive (R1) and the conductive (C1–C3) anomalies shown in Plate 2b has been scrutinized by forward modelling. A manual, subsequent removal of the anomalies R1, C1, C2 and C3 leads, in all case except C2, to an increase in rms misfit between observed data and model response, indicating that, except C2, the resistive anomaly R1 and conductive anomalies C1 and C3 are well constrained by the MT data. In contrast to profile A the WFZ (C3) is sensed on profile B by both polarizations. However, the horizontal and vertical extend of WFZ on profile B is only poorly resolved due to the lack of site coverage in this part of the profile. The estimated static shift values are displayed in Plate 2d. Strong static shifts for E- and B-Pol apparent resistivities have been observed at sites close to the LVZ and WFZ fault traces. Rms misfits are calculated from phase data only and are distributed fairly evenly along the profile (Plate 2c) yielding to an average rms of 1.55 (assuming a 2.86° error-floor for the phase data). The observed data and model response pseudo-sections are given in Plate 2e.

5. Discussion

5.1. The structure and geometry of the West Fissure Zone

The subdivision of fault zones into three units defined by

Fig. 7. Fracture and vein orientation along profiles A and B. (a) Histograms of fracture orientation in dependence of fault distance (normal to the fault trace) for profile A. *y*-axis: number of fractures, *x*-axis: fracture orientation in degree × 10^1. (b) Stereonets show vein orientation for profile A. (c) Histograms of fracture orientation in dependence of fault distance (normal to the fault trace) for profile B. The numbers in the circles represent the investigated locations.

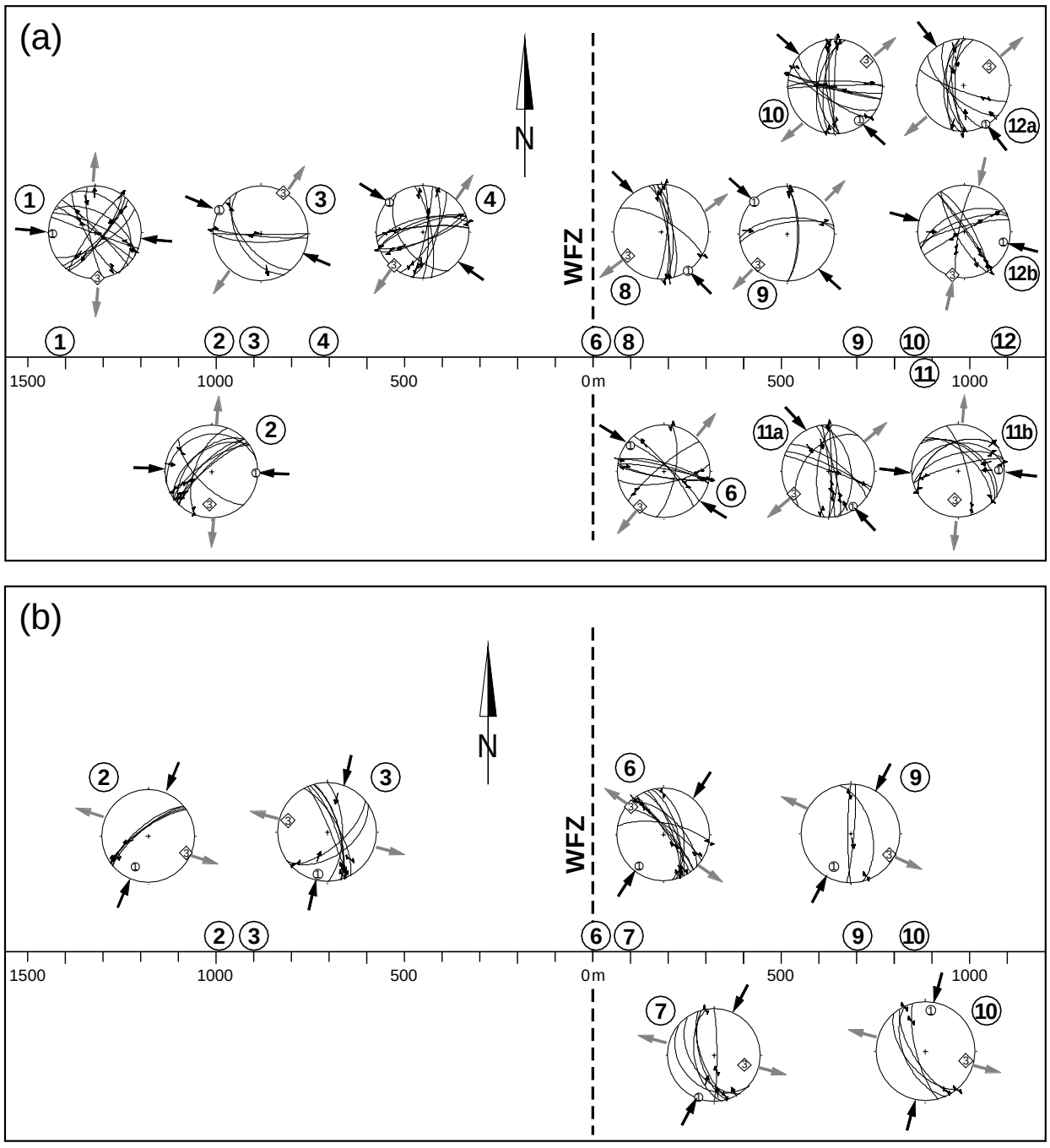

Fig. 8. Fault planes and fault slip data. The lines indicate the orientation of the average main fault traces; the dots indicate the striation directions measured on the fault plane; the small arrows (within the plot) represent the sense of slip of the hanging wall and large arrows and the numbers 1 and 3 depict the shortening and extension directions, respectively. (a) Orientation of principal strain axes for the older event in profile A. (b) Orientation of principal strain axes for the younger event in profile A. The numbers in the circles represent the investigated locations. (c) Orientation of principal strain axes for profile B. Asterisks indicate AMT sites.

relative deformation intensity (the fault core or main gouge zone, the fault damaged zone and undeformed host rock) as it is discussed in many papers could be recognised at macroscopic scale. However, the boundaries between the units are not distinct. Rather, the transition is gradual and not always clearly observable. A main gouge zone and cataclastic series, which in general build up the fault core (e.g. Chester and Logan, 1986; Caine et al., 1996), are not exhibited. This observation is contrary to other segments of the WFZ (e.g. close to the Chuquicamata copper mine) where gouge zones ranging from millimetres to >2 m and cataclastic series are developed (Reutter et al., 1996).

There is a distinct correlation between fracture densities, kinematic analysis and AMT data. The width of the fault,

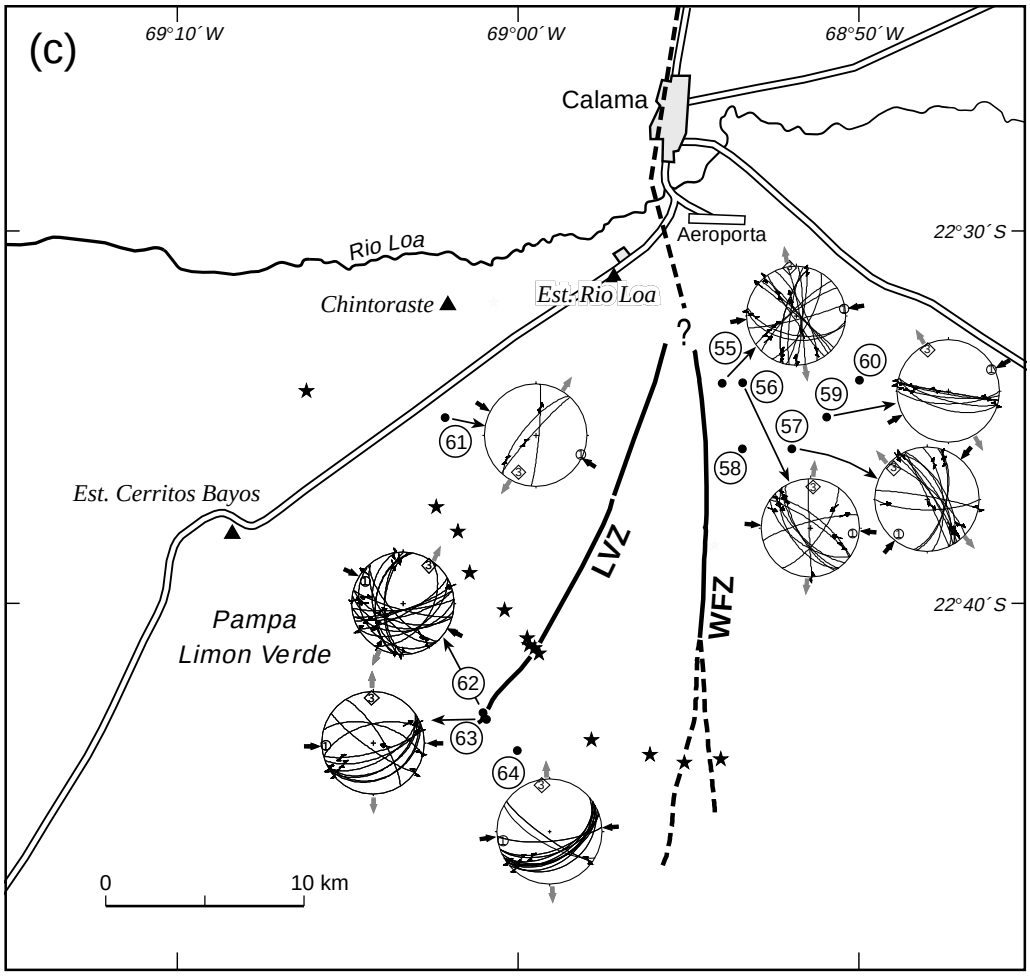

Fig. 8. (*continued*)

defined as a zone of increased fracture density, is about 4000 m for profile A (first row in Fig. 10a) and 7000 m for profile B (first row in Fig. 10b). The broader zone of profile B is probably caused by the interaction of the two fault branches WFZ and LVZ (see Schulz and Evans, 2000). The kinematic analysis based on fault slip data confirms the result of the aerial photograph analysis: the differentiation between the fault-related damaged zone and the host rock is marked by a significant change in orientation of principal strain axes (second row in Fig. 10a and b). Hence, we suggest that the zone where the fault is kinematically coherent also represents the fault zone width. Comparing profiles A and B, we observe the same tendency along both profiles.

The AMT imaging shows low electrical resistivity zones (apparent resistivities below 20 and 50 Ωm, respectively) that match the fault core defined by fracture density (third row in Fig. 10a and b). These conductive zones are very narrow (100–200 m) and extend to shallow depths only (50 m in profile A, 200 m in profile B). They may mark the regions of fluid penetration, most likely meteoric water, into the ruptured fault core (see Unsworth et al., 1997). Localised formation of clay-rich gouge zones might be another cause for reduced resistivities because clay is usually a good conductor (1–10 Ωm). Laboratory experiments of electrical resistivities of a sand–clay mixture by Wildenschild et al. (2000) show that a sand–clay mixture of 3–10% clay and 30% porosity filled with slightly saline fluids (fluid resistivities in the range of 5 to 20 Ωm) may explain the observed subsurface resistivities within the range of 10 to 50 Ωm. Higher saline and therefore less resistive fluids would require less pore space.

However, these narrow conductive zones extending to shallow depth contrast with the broad damaged zone revealed by the structural analysis and with results of other magnetotelluric investigations (Eberhart-Philips et al., 1995; Unsworth et al., 2000). Unsworth et al. (2000), for example, have described a zone of low electrical resistivity, which is several hundred metres wide and extends to a depth of about 4000 m for the Parkfield segment of the San Andreas Fault. The absence of a deep reaching conducting zone (profile A) or even the existence of its high resistive complement (profile B) let us assume that an impermeable seal at the WFZ prevents the expanded infiltration of meteoric water (see Section 5.3).

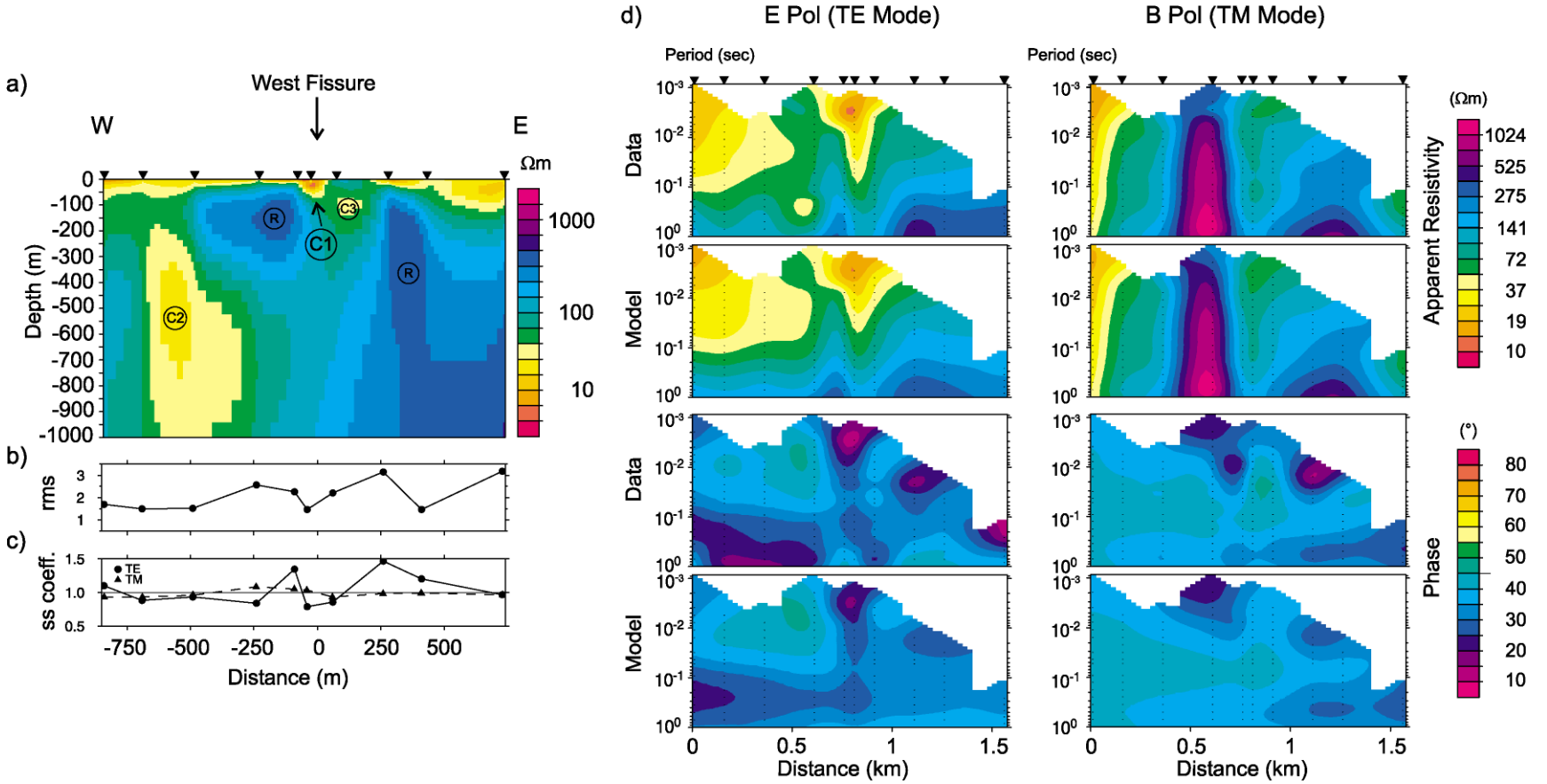

Plate 1. Joint E- and B-Pol data inversion results of the Guatacondo AMT survey. (a) Inversion model shown without vertical exaggeration. In the position of the surface trace of the West Fissure Fault a shallow good conducting anomaly (C1) is visible down to 50 m, which is flanked by two resistive zones (R). No further anomaly is imaged at greater depth. The shapes of the conductivity anomalies C2 and C3 are not well constrained. The two diagrams below show the root mean square misfit for each site ((b), overall rms: 2.06) and the static shift coefficients for TE- and TM-modes separately (c). Non shifted sites have a value of one; the original data are shifted to higher apparent resistivity values if the static shift coefficient is greater than one and vice versa. (d) Pseudo-sections of static shift corrected apparent resistivities and phases of measured and modelled data for both polarisations.

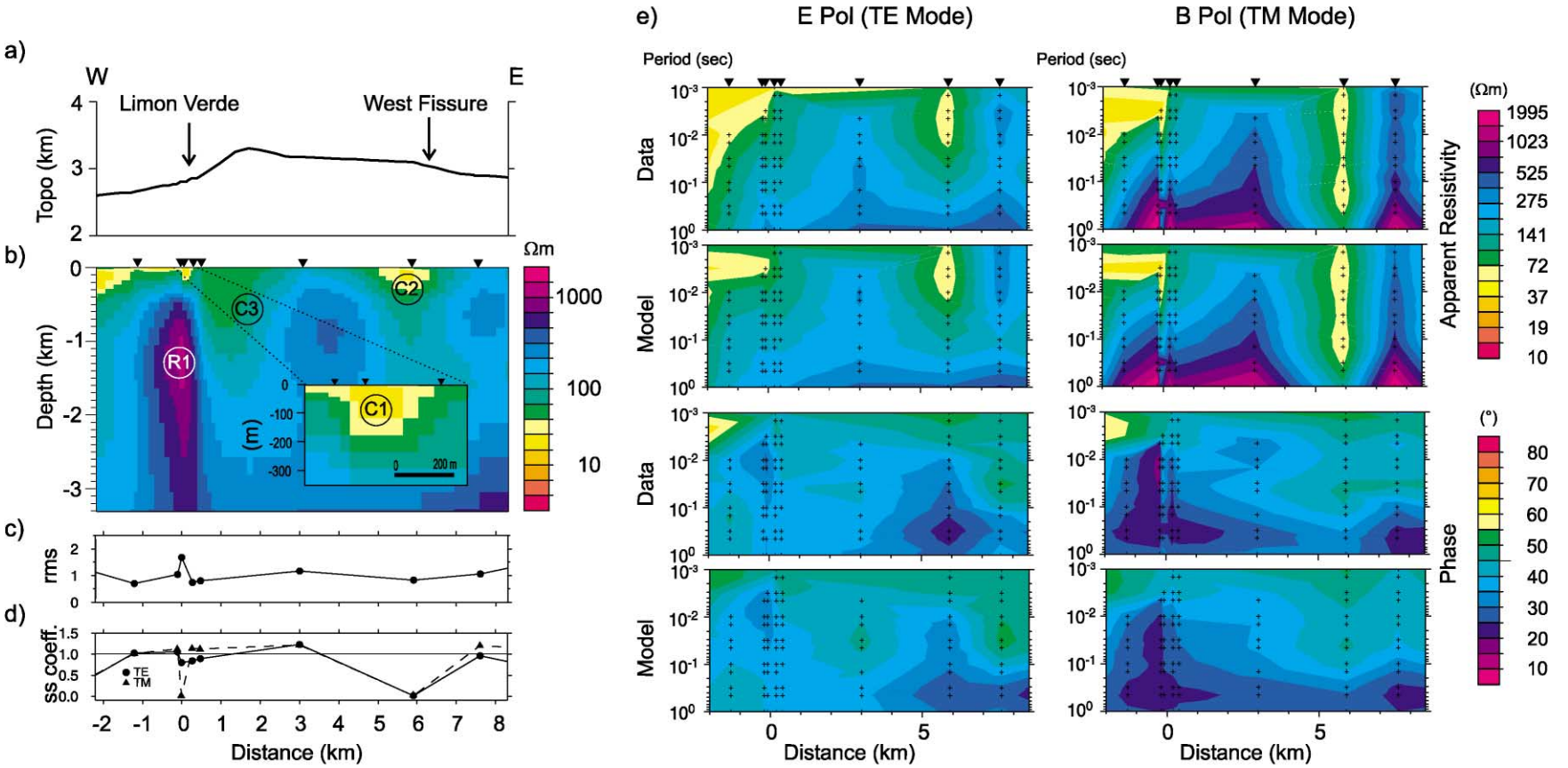

Plate 2. Joint E- and B-Pol data inversion results of the Limon Verde AMT survey. (a) Topography. (b) Inversion model shown with a vertical exaggeration of two. The inset gives a detail of model (without vertical exaggeration). The trace of the Limon Verde Fault zone (LVZ) coincides with a good conductor (C1) at shallow depth (<200 m). At greater depth the LVZ is underlain by a resistive zone (R1). The trace of the West Fissure Fault coincides with a modest conductivity anomaly (C3), but the shape and conductivity of C3 is not well constrained. The existence of C2 is uncertain. (c) Shows the root mean square misfit calculated from phase data only for each site (average rms: 1.55, overall rms: 2.69). (d) Static shift coefficients for TE- and TM-modes (cf. Plate 1). (e) Pseudo-sections of static shift corrected apparent resistivities and phases of measured and modelled data for both polarisations.

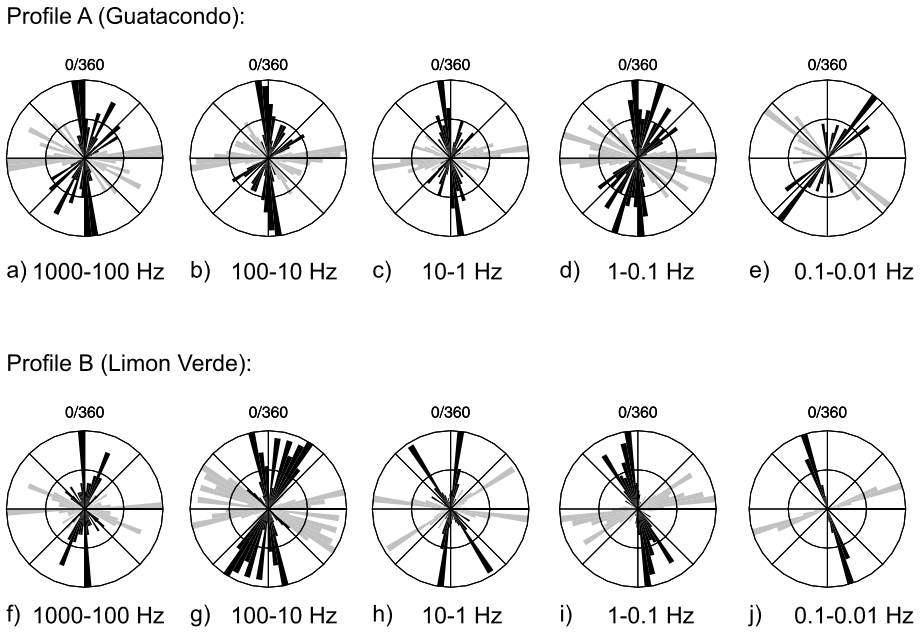

Fig. 9. Determination of AMT strike direction for profile A after Swift (1967) (a–e) and for profile B after Groom and Bailey (1989) (f–j). Data plotted as normalized polar histograms; grey colors denote the 90° ambiguity of the strike estimates. Decreasing frequency corresponds to increasing penetration depths. For profile A a strike angle of 5°W dominates the three highest frequency bands (a–c). For the Limon Verde profile the strike directions varies around a northerly orientation (see text).

In summary, our estimated fault thickness is in agreement with recent work of others authors (e.g. Schulz and Evans, 1998, 2000) who show that fault thickness depends on the type of signatures (mesoscopic structures, kinematic patterns, AMT surveys), as well as the scale of observation.

5.2. Scaling relationship

The cohesion-zone fault growth model (Cowie and Scholz, 1992; Scholz et al., 1993) predicts that longer faults should have wider fracture process zones (fault widths) since the zone of inelastic yield increases with fault length. The authors postulate that the ratio between the width of the fault (W_f) and the length of the fault (L) is approximately 0.15–0.2. Vermilye (1996) and Vermilye and Scholz (1998) estimated a ratio of 0.01 for several metre-scale faults. In order to test the theoretical predictions proposed by Cowie and Scholz (1992) and the ratios estimated by Vermilye and Scholz (1998) we calculated the ratio W_f/L for profiles A and B using the fault width estimates from aerial photographs.

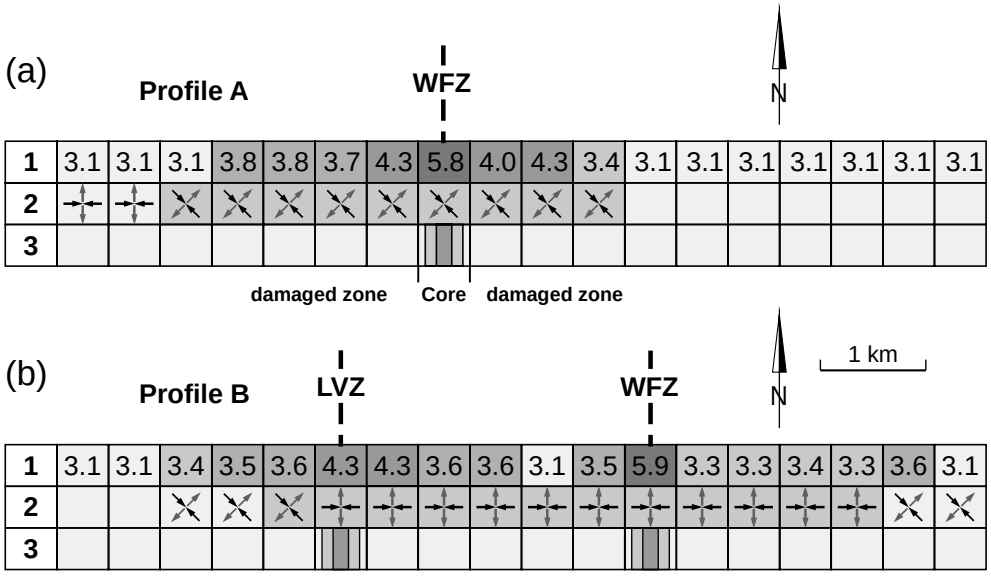

Fig. 10. Comparison of fracture density (1), orientation sketches of principal strain axes (2) and the thickness of the zone of low electrical resistivity (3). (a) Profile A. (b) Profile B.

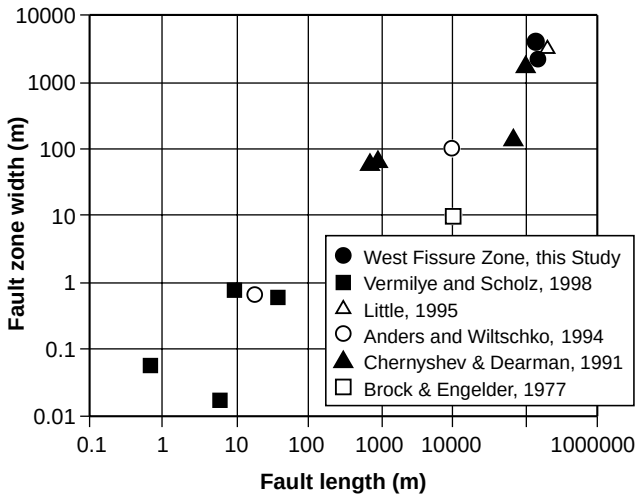

Fig. 11. Plot of process zone (fault thickness) width versus fault length for this study and additional published data. (Brock and Engelder, 1977. Chernyshev and Dearman, 1991. Little, 1995.)

The exposed fault length is estimated to be 170 km (Dilles et al., 1997) and the fault width is measured as 4000 m for profile A and 7000 m for profile B (see above). The calculated ratios of fault width to fault length (W_f/L) fall within the order of 10^{-2} (0.024 and 0.041, Table 1), which compares favourably with measured ratios from other natural fault zones (Fig. 11). However, it should be noted that the data from natural faults are at least one order of magnitude smaller than the values estimated by Cowie and Scholz (1992). We assume that values from natural fault zones represent lower limits because the superimposition of background fracture density together with a lack of outcrops can make fault deformation at greater distance of the fault core undetectable.

Furthermore Cowie and Scholz (1992) and Scholz et al. (1993) also predicted a positive linearly scaling between the fault (process zone) width (W_f) and the fault displacement (d). Because we were not able to measure the fault displacement directly, we used their inferred ratio ($W_f/d = 10–10^{-1}$) in order to estimate the displacement. Using the estimated fault width of 7000 m and the ratio W_f/d in the order of 10^{-1} (0.2) we calculated a displacement of approximately 35 km (Table 1) that agrees with the suggested maximum strike-slip displacement based on geological mapping (Tomlinson et al., 1997a,b).

5.3. Fault zone evolution

Recent models of fault zone evolution propose a cyclic nature of earthquake faulting processes (Blanpied et al., 1992; Sibson, 1992; Sleep and Blanpied, 1992; Byerlee, 1993; Caine et al., 1996; Miller et al., 1996; Grey et al., 1999; Cello, 2000). This requires the repeated destruction and creation of permeability within the fault zone causing weakening and hardening processes, respectively. Relating this to fluids, cyclic development implies a repeated change between an open and closed system during co-seismic and inter-seismic periods, respectively.

When reconciled with fault zone models our work may indicate an inter-seismic period of cyclic fault evolution for the investigated portions of the WFZ/LVZ. According to these models, faults are characterised by an impermeable seal due to compaction and cementation in the inter-seismic period. This assumption is consistent with our field observation and the AMT results (Plates 1 and 2). The geometry of the two magnetotelluric anomalies within the WFZ/LVZ reveals zones of slightly increased conductivity, which are narrow and do not reach deeply. If fluids are responsible for this conductivity enhancement, then reduced permeability would appear to prohibit fluid circulation at greater depth. Fluids and fluid transport are confined to the remaining fractures within the fault core at shallow depth. These observations are similar to those described by Mackie et al. (1997b) and Unsworth et al. (1999) for the Carrizo Plain Segment of the San Andreas Fault (SAF). Here, an anomalous conductive zone, comparable with the Parkfield segment mentioned above could not be proven. The authors assume that seismic quiescence (the Carrizo Plain segment has been seismically locked since 1857) and the lack of dominant conductivity enhancement are connected with reduced fluid flow. Unfortunately, there are no records of the past seismicity along the investigated WFZ-segments. Ongoing investigation of upper crustal seismicity show no clustering of seismic events along the fault traces (Arturo Belmonte, pers. commun., 2001). Judging from the magnetotelluric results the healing of the damaged zone has evolved much further than at the Carrizo Plain segment of the SAF.

However, for a fault length of 170 km it seems reasonable to assume that the fault transects the upper brittle part of the crust (down to 15–20 km). It is entirely possible that fault sealing is only effective in the upper few kilometres of the crust. This might be indicated by long period magnetotelluric measurements (having greater depth resolution) along a profile, which passes profile A (Brasse et al., 2001). These MT results show a good conductor (the Precordilleran Fault system?) at a depth of ~20 km without transition to the uppermost crust.

6. Conclusions

Geological field work, insights from aerial photographs and kinematic data from two profiles across the WFZ in northern Chile reveal a broad damaged zone and a fault core that is characterised by the increase in subsidiary faults above regional levels and not composed of gouge and cataclastic series as described for other fault zones. These observations are supported by AMT data indicating a narrow zone of low resistivity.

The width of WFZ defined by fracture density (derived from aerial photographs) is about 4000 m for profile A and

7000 m for profile B. These widths correspond roughly to the regions where the fault is kinematically uniform. The calculated ratio between fault width (W_f) and fault length (L) fall within the order of 10^{-2}, which compares favourably with the measured ratios on small natural fault zones (Vermilye and Scholz, 1998).

The audiomagnetotelluric low electrical resistivity zones are congruent with the fault core defined by fracture density. These zones are only 100–200 m wide and 50 and 200 m deep, respectively. We suggest that fluids and fluid transport, which are probably responsible for enhanced conductivity, are confined to the fault core at shallow depth because of missing conduit behaviour of the fault during the inter-seismic period of fault evolution.

Acknowledgements

We have to thank many co-workers for their help in the field, namely J. Beike, F. Echternacht, M. Eisel, S. Friedel, W. Heise, P. Lezaeta, K. Schwalenberg and W. Soyer. We gratefully acknowledge the support of G. Behn (Codelco Chile), G. Chong Diaz (Univ. Catilica del Norte, Antofagasta), L. Baeza (Codelco Chile). Special thanks are addressed to H. Brasse and G. Dresen for their constructive criticisms. We thank A. Hendrich for help with drafting. J.P. Evans, D.R. Grey and M.J. Unsworth provide constructive reviews that significantly improved the manuscript. This work was funded by the the DFG (German Research Foundation) within the framework of the Collaborative Research project SFB 267 Deformation Processes in the Central Andes and by the GeoForschungsZentrum Potsdam.

References

Allmendinger, R.W., 1989. Notes on Fault Slip Analysis: Short Course "Quantitative Interpretation of Joints and Faults". Cornell University, Ithaca, NY.

Anders, M.H., Wiltschko, D.V., 1994. Microfracturing, paleostress and the growth of faults. Journal of Structural Geology 16, 95–815.

Baeza, L., 1984. Petrography and tectonics of the plutonic and metamorphic complexes of Limón Verde and Mejillones Peninsula, Northern Chile. PhD Thesis. Eberhard-Karls-Universität, Tübingen.

Beck, M.E., 1983. On the mechanism of tectonic transport in zones of oblique subduction. Tectonophysics 93, 1–11.

Blanpied, M.L., Lockner, D.A., Byerlee, J.D., 1992. An earthquake mechanism based on rapid sealing of faults. Nature 358, 574–576.

Boric, R., Diaz, F., Maksaev, V., 1990. Geologia y Yasimientos Metaliferos de la Region de Antofagasta. Serv. Nac. Miner. Santiago, 40.

Brasse, H., Leazaeta, P., Rath, V., Schwalenberg, K., Soyer, W., Haak, V., 2001. The Bolivian Altiplano conductivity anomaly. Journal of Geophysical Research in review.

Brock, W.G., Engelder, J.T., 1977. Deformation associated with the movement of the Muddy Mountain overthrust in the Buffington window, southeastern Nevada. Bulletin Geological Society of America 88, 1667–1677.

Byerlee, J., 1993. Model for episodic flow of high-pressure water in fault zones before earthquakes. Geology 21, 303–306.

Caine, J.S., Evans, J.P., Forster, C.B., 1996. Fault zone architecture and permeability structure. Geology 24, 1025–1028.

Carrasco, P., Wilke, H., Schneider, H., 1999. Post-Eocene deformational events in the North segment of the Precordilleran Fault system, Copaquiri (21°S). Fourth ISAG, Göttingen (Germany), 04-06/10/99.

Cello, G., 2000. A quantitative structural approach to the study of active fault zones in the Apennines (Peninsular Italy). Journal of Geodynamics 29, 265–292.

Chernyshev, S.N., Dearman, W.R., 1991. Rock Fractures. Butterworth-Heinemann, Newton, MA.

Chester, F.M., Logan, J.M., 1986. Implication for mechanical properties of brittle faults from observations of Punchbowl fault zone, California. Pure Applied Geophysics 12, 79–106.

Chester, F.M., Evans, J.P., Biegel, R.L., 1993. Internal structure and weakening mechanisms of the San Andreas Fault. Journal of Geophysical Research 98, 771–786.

Coira, B., Davidson, J., Mpodozis, C., Ramos, V., 1982. Tectonic and magmatic evolution of the Andes of northern Argentina and Chile. Earth Science Review 18, 303–332.

Cowie, P.A., Scholz, C.H., 1992. Physical explanation for displacement-length relationship of faults using a post-yield fracture mechanics model. Journal of Structural Geology 14, 1133–1148.

Cowie, P.A., Shipton, Z.K., 1998. Fault displacement gradients and process zone dimensions. Journal of Structural Geology 20, 983–997.

Dilles, J.H., Tomlinson, A.J., Martin, M.W., Blanco, N., 1997. El Abra and Fortuna Complexes: a porphyry copper batholit sinistrally displaced by the Falla Oeste. Actas 8th Congr. Geol. Chile, Antofagasta, v. III, pp. 1883–1887.

Eberhart-Philips, D., Stanley, W.D., Rodriguez, B.D., Lutter, W.J., 1995. Surface seismic and electrical methods to detect fluids related to faulting. Journal of Geophysical Research 100, 12,919–12,936.

Grey, D.R., Janssen, C., Vapnik, Y., 1999. Deformation character and palaeo-fluid flow across a wrench fault within a Palaeozoic subduction-accretion system: Waratah Fault Zone, southeastern Australia. Journal of Structural Geology 21, 194–214.

Groom, R.W., Bailey, R.C., 1989. Decomposition of magnetotelluric impedance tensors in presence of local three-dimensional galvanic distortion. Journal of Geophysical Research 94, 1913–1925.

Hammerschmidt, K., Döbel, R., Friedrichsen, H., 1992. Implication of $^{40}Ar-^{39}Ar$ dating of Early Tertiary volcanic rocks from the north-Chilean Precordillera. Tectonophysics 202, 241–247.

Jones, A.G., 1988. Static shift of magnetotelluric data and its removal in a sedimentary basin environment. Geophysics 53, 967–978.

Lachenbruch, A.H., Sass, J.H., 1980. Heat flow and energetics of the San Andreas fault zone. Journal Geophysical Research 85, 6185–6622.

Lindsay, D.D., Zentilli, M., Rivera, A.J., 1995. Evolution of an active ductile to brittle shear system controlling mineralization at Chuquicamata porphyry copper deposit, Northern Chile. International Geology Review 37, 945–958.

Little, T.A., 1995. Brittle deformation adjacent to the Awatere strike-slip fault in New Zealand: faulting patterns, scaling relationships, and displacement partitioning. Bulletin Geological Society of America 107, 1255–1271.

Lucassen, F., Franz, G., Laber, A., 1999. Permian high pressure rocks—the basement of the Sierra de Limon Verde in Northern Chile. Journal of South American Earth Sciences 12, 183–199.

Mackie, R.L., Rieven, S., Rodi, W., 1997a. Users Manual and Software Documentation for Two-Dimensional Inversion of Magnetotelluric Data. Department of Geological Sciences, Indiana University, Bloomington, IN.

Mackie, R.L., Livelybrooks, D.W., Madden, T.R., Larsen, J.C., 1997b. A magnetotelluric investigation of the San Andreas fault at Carrizo Plain, California. Geophysical Research Letters 24 (15), 1847–1850.

Michel, G.W., 1994. Neo-kinematics along the North-Anatolian Fault (Turkey). Tübinger Geowissenschaftliche Arbeiten, Reihe A, 16.

Miller, S.A., Nur, A., Olggaard, D.L., 1996. Earthquakes as a coupled shear

stress — high pore pressure dynamical system. Geophysical Research Letters 23, 197–200.

Molnar, P., 1992. Brace-goetze strength profiles, the partitioning of strike-slip and thrust faulting at zones of oblique convergence, and the stress-heat flow paradox of the San Andreas Fault. In: Evans, B., Wong, T.F. (Eds.), Fault Mechanics and Transport Properties of Rocks. Academic Press, London, 435–459.

Muñoz, N., Sepulveda, P., 1992. Estructuras con vergencial al oeste en el borde oriental de la Depresión Central, Norte de Chile (19°15′S). Revista Geológica de Chile 19, 241–247.

Reutter, K.J., Scheuber, E., Helmcke, D., 1991. Structural evidence of orogen-parallel strike slip displacements in the Precordillera of northern Chile. Geologische Rundschau 80, 135–153.

Reutter, K.-J., Döbel, R., Bogdanic, T., Kley, J., 1994. Geological map of the central Andes between 20°S and 26°S. In: Reutter, K.-J., Scheuber, E., Wigger, P. (Eds.), Tectonics of the Southern Central Andes. Springer, Heidelberg.

Reutter, K.-J., Scheuber, E., Chong, G., 1996. The Precordilleran fault system of Chuquicamata, Northern Chile: evidence for reversals along arc-parallel strike-slip faults. Tectonophysics 259, 213–228.

Scheuber, E., Bogdanic, T., Jensen, A., Reutter, K.-J., 1994. Tectonic development of the North Chilean Andes in relation to plate convergence and magmatism since the Jurassic. In: Reutter, K.-J., Scheuber, E., Wigger, P. (Eds.), Tectonics of the Southern Central Andes. Springer, pp. 121–239.

Scholz, C.H., Dawers, N.H., Yu, J.Z., Anders, M.H., Cowie, P.A., 1993. Fault growth and fault scaling laws: preliminary results. Journal of Geophysical Research 98, 21951–21961.

Schulz, S.E., Evans, J.P., 1998. Spatial variability in microscopic deformation and composition of the Punchbowl fault, southern California: implications for mechanisms, fluid-rock interactions, and fault morphology. Tectonophysics 295, 223–244.

Schulz, S.E., Evans, J.P., 2000. Mesoscopic structure of the Punchbowl Fault, Southern California and the geologic and geophysical structure of active strike-slip fault. Journal of Structural Geology 22, 913–930.

Shipton, Z.K., Cowie, P.A., Vermilye, J., 1997. Fault displacement profiles and off-fault damaged, interpreting the record of fault growth. Abstracts of Proceedings, Geological Society of America (GSA), 199.

Sibson, R.H., 1992. Implications of fault-valve behaviour for rupture nucleation and recurrence. Tectonophysics 192, 283–293.

Sleep, N.H., Blanpied, M.L., 1992. Creep, compaction and the weak rheology of major faults. Nature 359, 687–692.

Swift, C.M., 1967. A Magnetotelluric Investigation of an Electrical Conductivity Anomaly in the Southwestern United States. PhD thesis, Massachusetts Institute of Technology, Cambridge.

Tomlinson, A.J., Blanco, N., 1997a. Structural evolution and displacement history of the west fault system, Precordillera, Chile: Part 1, synmineral history. Actas 8th Congr. Geol. Chile, Antofagasta, v. III, pp. 1883–1887.

Tomlinson, A.J., Blanco, N., 1997b. Structural evolution and displacement history of the west fault system, Precordillera, Chile: Part 2, postmineral history. Actas 8th Congr. Geol. Chile, Antofagasta, v. III, pp. 1878–1882.

Underwood, E.E., 1970. Quantitative Stereology. Addison-Wesley, Reading, MA, p. 274.

Unsworth, M.J., Malin, P.E., Egbert, G.D., Booker, J.R., 1997. Internal structure of San Andreas fault at Parkfield, California. Geology 25, 359–362.

Unsworth, M.J., Egbert, G.D., Booker, J.R., 1999. High-resolution electromagnetic imaging of the San Andreas fault in Central California. Journal of Geophysical Research 104, 1131–1150.

Unsworth, M.J., Bedrosian, P., Eisel, M., Egbert, G.D., Siripunvaraporn, W., 2000. Along strike variations in the electrical structure of the San Andreas Fault at Parkfield, California. Geophysical Research Letters 27 (18), 3021–3024.

Vergara, H., Thomas, A., 1984. Hoja Collagua, Region de Tarapaca Carta Geologica de Chile. Servico Nacional de Geologia y Mineria 59, 1–79.

Vermilye, J.M., 1996. The Growth of Natural Fracture Systems: A Fracture Mechanics Approach. PhD thesis, Columbia University.

Vermilye, J.M., Scholz, C.H., 1998. The process zone: a microstructural view of fault growth. Journal of Geophysical Research 103, 12223–12237.

Vermilye, J.M., Scholz, C.H., 1999. Fault propagation and segmentation: insight from the microstructural examination of a small fault. Journal of Structural Geology 21, 1623–1636.

Wildenschild, D., Roberts, J.J., Carlberg, E.D., 2000. On the relationship between microstructure and electrical and hydraulic properties of sand–clay mixtures. Geophysical Research Letters 27 (19), 3085–3088.

Zoback, M.D., Zoback, M.L., Mount, V.S., Suppe, J., Eaton, J.P., Healy, J.H., Oppenheimer, D., Reasenberg, P., Jones, L., Raleigh, C.B., Wong, I.G., Scotti, O., Wentworth, C., 1987. New evidence on the state of stress on the San Andreas fault system. Science 238, 1105–1111.